Fabio Cufino - Angelo Arisi

Advisor: Your Advisor ?????

Advanced Laboratory course:
Particle physics

Scintillating Fibers

October 15, 2024

technische universität
dortmund

Abstract

Scintillating fibers play a vital role in particle physics experiments, serving as tracking detectors to record the trajectories of charged particles. This report investigates the properties of scintillating fibers within the context of the LHCb experiment at TU Dortmund University. The study focuses on understanding the behavior of photons within the fibers through both simulation and experimental measurements. Monte Carlo simulations using Geant4 are employed to model the interaction of photons with the fibers, providing insights into their transport and detection. Experimental setups are utilized to validate simulation results and assess the performance of the fibers in detecting ionizing radiation. Key parameters, including photon paths, reflections, and energy deposition, are analyzed to characterize the behavior of scintillating fibers.

Table of contents

1 Introduction

Tracking detectors are fundamental in particle physics, enabling the reconstruction of charged particle paths and property identification. Scintillating fibers used for this experience are a versatile tracking technology. They offer high spatial resolution and efficient photon detection, ideal for precise tracking.

Scintillating fibers are used within the LHCb experiment. Through spectrometer measurements of a single fiber and Monte Carlo simulations, we aim to understand behaviour of the photons generated by the fibers, and some of the fundamental property of this detection method, including interaction, detection efficiency, and energy deposition.

The next section shortly introduces LHCb experiment with a focus on scintillating fibers. Secondly a brief excursus on the experimental apparatus and the scintillation mechanism will be done, introducing the necessary concepts and physical quantities to understand the experiment. Section 4 is dedicated to the analysis and the results of both the experiment and the simulation.

2 The LHCb experiment

The LHCb detector, situated at the Large Hadron Collider (LHC) at CERN, Geneva, Switzerland, is an essential component in the exploration of particle physics. Its primary mission is to investigate the subtle differences between matter and antimatter by studying CP violation in the behaviour of particles containing b and c quarks. These particles play a crucial role in our understanding of the universe's fundamental forces and the prevalence of matter over antimatter.

The LHCb detector is a single-arm forward spectrometer and is shown in Figure 1.

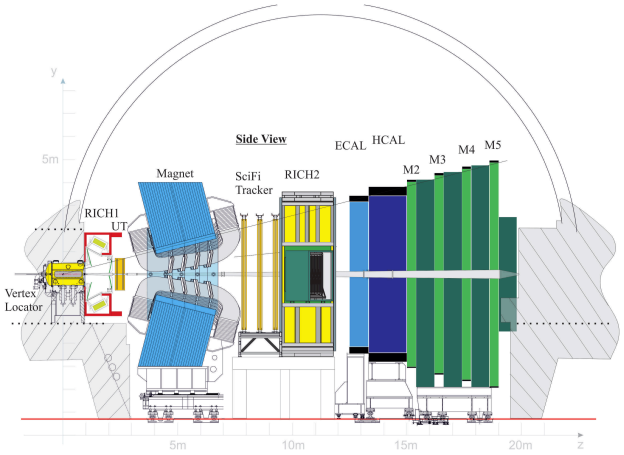

Figure 1: Schematic side-view of the planned upgraded LHCb detector. UT = Upstream Tracker. SciFi Tracker = Scintillating Fibre Tracker.

A right-handed coordinate system is used for its description. The z-axis is in the direction

of the beam while the x and y axis are perpendicular to it, with the y being the vertical axis. At the LHC, the particles LHCb wants to study are produced with a strong boost in the forward direction along the direction of the proton beams. The decay products of these particles can be observed at a polar angle of $15-300mrad$. Hadrons with b quarks travel a few millimeters to a few centimeters before decaying because of their relatively high lifetime. The aim of LHCb are precision measurements so it is fundamental to have a high-precision tracking system to reconstruct the tracks of the hadron produced. This is composed, before the magnet, by the vertex locator (VELO), which reconstructs the point of the p-p interaction and the primary vertex, and the Trigger Tracker, a large area of silicon strip detectors. While after the magnet is placed the Scifi Tracker.

3 Scintillating Fibre Tracker

The Scintillating Fiber Tracker (SciFi Tracker) with respect to the previous tracking stations of silicon strip detectors, can achieve higher resolution, up to $100\mu m$, and is also much more inexpensive to manufacture, so it can easily cover a very large area.

The fibers in the detector are processed into *fibre mats*. A single mat is an hexagonal structure of fibers held together by Epoxy glue. The tracking system consists of three stations T1, T2 and T3, each consisting of four layers of mats arranged one behind the other, each layer containing around 40 mats.

The fibers have a polystirene core which measures $2.5m$ in length and $220m$ in thickness. The polystirene is an organic scintillator which is the active detector medium. Surrounding the core, there are two sheaths with refractive indices that decrease outwardly, enabling total internal reflection at the interfaces. Each sheath has a thickness of $7.5m$, resulting in a total thickness of $250m$. The refractive indexes of the core, cladding and outer sheath are respectively $n = 1.60$, $n = 1.49$ and $n = 1.42$.

The fibers are strategically positioned within the detector to intercept charged particles traversing the experimental apparatus. The layout of the SciFi Tracker is shown in Figure 2

The photon generated are readout through silicon pixels placed at the outer ends of the mats.

3.1 Simulation

In particle physics Monte Carlo simulations are very useful to study the properties and performance of particle tracking subdetectors, before they are used or even built. For this experiment a simulation that takes into account a single fibre is used. The data from the single fibre simulation can be later used to make statements about the entire subdetector with another simulation. The success of the simulation highly depends on the accuracy with which every physical process and the apparatus' characteristics are represented. The single fibre simulation used here is implemented in Geant4 and simulates single photons travelling through the fibre. The various interaction mechanisms, such as Rayleigh scattering, attenuation in the materials and reflections at the interfaces, are considered. The simulation

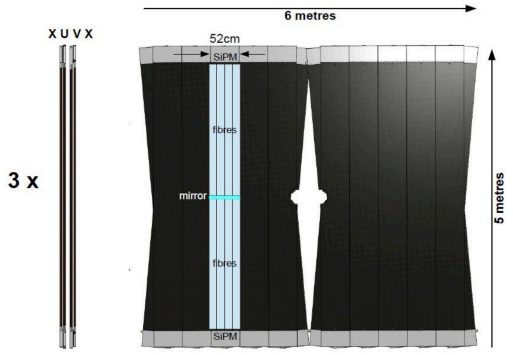

Figure 2: Schematic yz- and xy-view of one of the planned SciFi Tracker stations. It is composed out of 4 stereo-layers with vertical (x) and rotated (u,v) fibre orientation. Each the layers is composed out of two half layers with 6 individual fibre modules

consists of 50 fibres being stimulated at 24 points each resulting then in 1200 text files containing individual simulations. The different features of the simulation data and further details are described in Section 4.

3.2 Scintillation mechanism

The scintillation mechanism is based on the excitation of valence $\pi - electrons$ electrons of the polystirene. These excited electrons transition to higher energy levels within the molecular structure of the polystyrene. Subsequently, rapid relaxation processes occur, with excitation energy transitioning into the S_{10} state radioationless. Eventually, this energy is released in the form of ultraviolet (UV) photons as the S_{10} state transitions back to the ground state S_{00}. Pure polystyrene exhibits a modest quantum yield, approximately 3%, which is the fraction of S_{10} states that transition with radiation to the ground state. This is due to the long average decay time and competitive radiationless transitions. The addition of dye p-terphenyl enhances significantly this yield by facilitating rapid relaxation processes.

The photons emitted by the p-terphenyl however, have an absorption length of about $1m$ which is not enough to assure the arrival of the photon at the end of the fiber ($2.5m$ long). To overcome these limitations, wavelength shifters like TPB (tetraphenyl-butadiene) are employed, which absorb and re-emit photons at longer wavelengths, where the attenuation length of the photon increases.

Fundamental geometrical quantities of the photons trajectories to evaluate are the path length L and the number of reflections N. For photons penetrating the cladding these are non trivial but for the photons remaining in the core they are easy to calculate and depend on the distance on the fibre axis x and the angle θ with the x-axis:

$$L = \frac{x}{cos(\theta)} \quad and \qquad N = \frac{x \tan(\theta)}{2\sqrt{r_{Kern}^2 - r_{min}^2}} \tag{1}$$

where r_{core} denotes the radius of the fiber's core and r_{min} is the smallest distance to the fiber's center which is a constant of the trajectory. The geometry of the photon's trajectory is shown below.

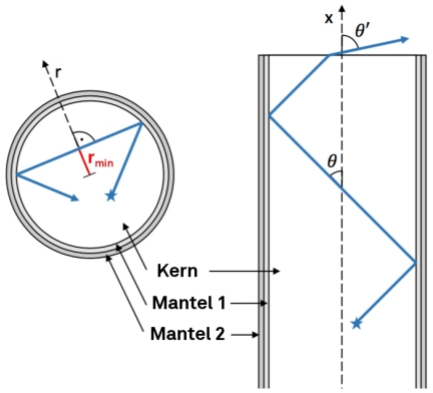

Figure 3: The path of a photon through the fiber. A trasversal cross-section of the fiber is shown on the left and r_min is highlighted. On the right a longitudinal section shows the same path and the angle θ with the central axis can be seen.

However r_{min} cannot be measured, therefore, it is necessary to find an average value for r_{min} from the simulation. Having the initial y and z position of the photons and the initial momentums p_y and p_z, and considering that the momentum are normalized, and so they give the initial direction of the line trajectory, r_{min} is the distance between such line and the center which can be calculated as:

$$r_{min} = \frac{|p_z y - p_y z|}{\sqrt{p_z^2 + p_y^2}} \tag{2}$$

For r_{min}, the photons move with helix trajectories and they remain in the fibre even with θ higher than angle of max reflection for flat trajectories. The angle to the interface infact can be calculated as:

$$\theta_{refl} = arcsin(\sqrt{1 - \frac{r_{min}}{r_{core}}} sin(\theta)) \tag{3}$$

and as we can see from the formula for r_{min} close to r_{core} θ_{refl} tends to 0° regardless of θ.

An other important phonomenon to be studied is attenuation. As photons traverse the fiber, some are absorbed or scattered through phenomena like Rayleigh scattering, molecular excitation and self-absorption of the wavelength-shifter. The intensity of the signal is then attenuated according to the exponential law:

$$I(x) = I_0 e^{-\frac{L}{\Lambda}} \tag{4}$$

where Λ represents the attenuation length or

$$I(x) = I_0 e^{-\frac{L}{a}} \tag{5}$$

where a is the attenuation coefficient. Moreover, the attenuation does not only come from internal absorption in the core but also from reflections at the core-cladding interface. The probability of such loss in a single reflection is determined by the reflection coefficient (ϵ). Considering both effects, the total intensity is expressed as:

$$I(x,\theta) = I_0 \cdot exp\left(-x\left(\frac{1}{\Lambda\cos\theta} + \frac{\epsilon\tan\theta}{2\sqrt{r_{core}^2 - r_{\min}^2}}\right)\right) \tag{6}$$

leading to an attenuation coefficient a described by:

$$a = \frac{1}{\Lambda\cos\theta} + \frac{\epsilon\tan\theta}{2\sqrt{r_{core}^2 - r_{\min}^2}} \tag{7}$$

4 Analysis

The analysis is logically divided in two parts: the analysis of the simulation data and the analysis of the measurements made in the lab.
The latter was done on a single scintillating fiber, excited with a LED light, and the photon were collected by a spectrometer. As a consequence the output for every measurement was a text file with two columns: the wavelength and the photon counts for the specific wavelength. For every measurement the current of the light was set at $20mA$, the total integration time at $10000ms$. The number of averages, which was set to 5 is the number of time the measurement is repeated and than the average of counts is taken. For every measurement (for example at a specific angle and excitation position) also the dark counts were taken: meaning taking a measurement with the same set up but with the LED off. In this way, subtracting for every wavelength the dark counts from the photon counts allows us to filter out the environmental photons not wanted for the analysis. During the analysis we never need the photon counts at a specific wavelength instead we just want the total photon counts, so for every specific setup of angle and excitation position we sum the counts we obtained from the subtraction with the dark counts and we refer to that as integrated intensity.

4.1 Spectrometer measurement

The behaviour of the scintillating fiber has been studied with a spectrometer to collect the produced photons and with an LED as a source. At first a spectrometer measurement is performed at a fixed low angle, in our case 0°, with the LED turned on and then turned off. As we mentioned before subtracting the counts of the dark counts from the one with the LED we filter out the environment photons.

We obtain a spectrum of the counts of the spectrometer as a function of the wavelength. The same measurement is carried out with and without room light, and since we environmental photons are not considered, the two spectra should look similar. The results is shown in Figure. 4.

We indeed notice in Figure 4 that the plots have the same shape. The oscillation in the light case is due to the statistical large amount of environmental photons with a specific λ that

Figure 4: Plot of the subtraction between the LED and the dark counts as a function of the wavelength. The pink and purple plots are respectively for the measure with room lights on and off.

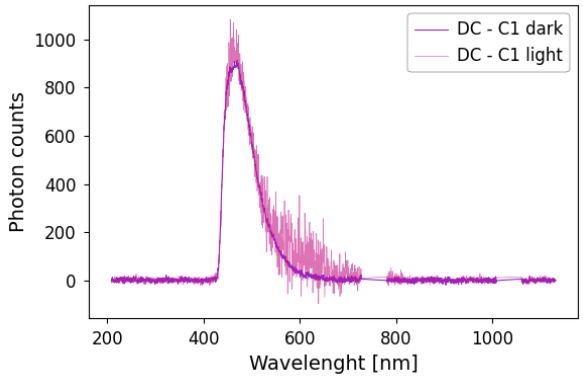

can fluctuate in time.

All the following measurement were performed with the room lights turned off in order to detect the least amount of external photons as possible.

4.2 Radial symmetry

Secondly the same measurement is repeated for different angles of the spectrometer, both horizontal and vertical. In this way the radial symmetry of the strip is being checked and verified. Small angles are also taken into consideration since the signal should be higher in those region. Due to the slight difference of ranges of the spectrometer the horizontal angle is analyzed from $-18°$ to $30°$ with steps of $4°$, while the vertical angle is taken from $-6°$ to $30°$ also with steps of $4°$.

In this case, for every couple of angle, the maximum intensity is taken instead of the integrated intensity. The plot of the maximum intensity as a function of the angles is shown in Figure 5.

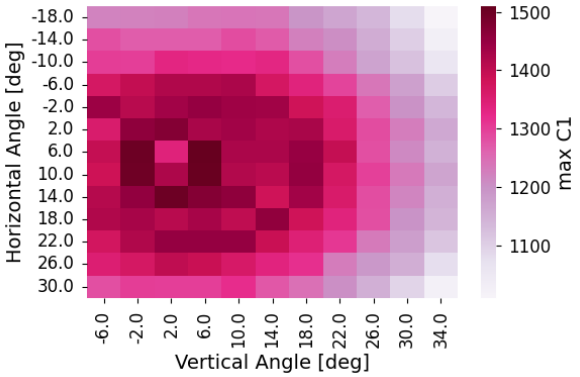

Figure 5: Heatmap of the integrated intensity as a function of the horizontal and vertical angle.

We can indeed observe the radial symmetry of the strip with the maximum intensity being detected at small exit angles indicatively from $2°$ to $10°$. The fact that the peak is not at $0°$

as we would expect is due to the spectrometer reference frame which is not perfectly centered with respect to the fiber.

4.3 X-dependent intensity

The intensity measurement was performed for different excitation position of the LED source. The vertical angle here is also changed, from 0° to 40° at steps of 4°. For every angle 20 excitation position are taken, from $x = 0mm$ to $x = 1900mm$ at steps of $100mm$. In Figure 6 is shown the 2D plot of the integrated intensity in terms of the angle and the excitation position.

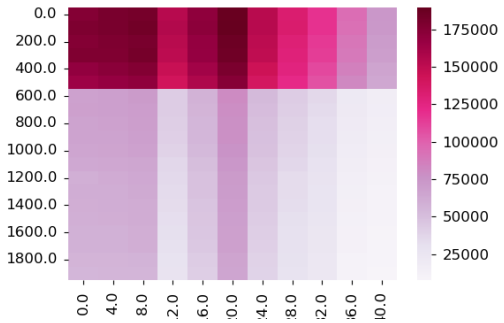

Figure 6: Heatmap of the integrated intensity in terms of the vertical angle and the excitation position. We notice an abrupt decrease of intensity at about $x = 550mm$.

As we saw before, the intensity peaks at angles close to 0 and decreases as the angle increases. However we notice an anomalous abrupt decrease of the intensity after $x = 550mm$. This is due to a physical rupture in the scintillating strip at that length that prevents most of the photon generated further to arrive at the end of the strip and be detected. This pattern is more recognizable in Figure 7, where we see the scatter plot of the intensity for different excitation positions at a single angle, at $\theta = 0\,\text{deg}$.

The purpose of the x-dependent intensity measure is to determine the attenuation coefficient since the intensity follows the negative exponential distribution:

$$I(x) = e^{-ax} \tag{8}$$

where a is the attenuation coefficient.
An exponential fit on our intensity data for the 20 x locations would provide us an estimation of a. Although, since the strip is broken between $500mm$ and $600mm$, only the first 6 points are used for the fit. As a consequence the fit will be very imprecise; nonetheless we obtain a physically acceptable result. For example for the vertical angle $v = 0$ we get $a = 1.30 \times 10^{-}4$.

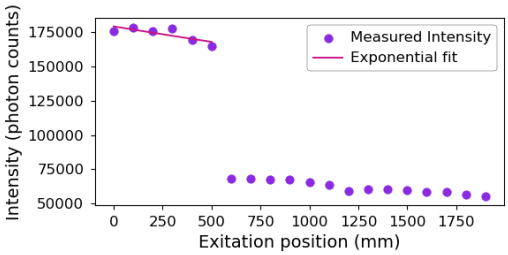

Figure 7: Scatter plot of the intensity for the 20 excitation position at the vertical angle of 0°. The exponential fit is performed only on the first 6 points.

The attenuation parameter is then computed for all the vertical angles considered and then plotted here in Figure 8.

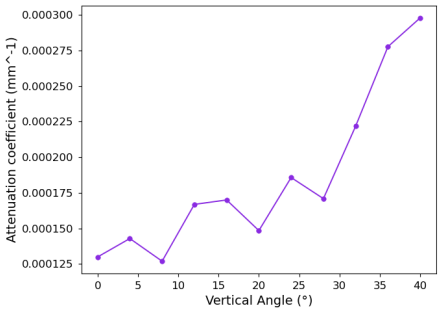

Figure 8: Plot of the attenuation parameter a in terms of the vertical angle. A clear increase of the attenuation with the angle is noticeable.

From the plot we observe an increase of the attenuation with the angle. This is expected and due to the fact that photon which have higher angles θ respect to the fiber axis are subject to more reflections and so have a longer path-length L. A higher L means higher probability of attenuation processes.

4.4 Angle dependent intensity

Finally a precise angle dependent intensity measurement is carried out in order to determine the most probable angle at which the photons exit the fiber. In order to find it the integrated intensity has been measured for every horizontal angle between 0° and 40°. Here the solid angle is considered meaning the intensity for a certain horizontal angle is weighted multiplying the intensity for the sine of the angle. The maximum intensity instead of the integrated intensity is also used in this case. The resulting plot is shown below in Figure 9. The behaviour is what we expected especially for low angles with the intensity increasing until the maximum angle of total reflection. Then, apart from a few outliers, we notice a decreasing tendency for higher angles as we should expect. The angle for maximum intensity is $\theta_{I_{max}} = 31°$ which is far from the theoretically calculated maximum angle of total reflection for the core photons $\theta_{max1} = 21.4°$ and for the cladding photons $\theta_{max1} = 27.4°$. However we notice how the correspondent bin is an outlier with respect of the adjacent bins, while the

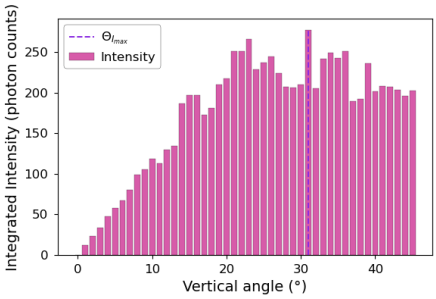

Figure 9: Plot of the intensity in terms of the horizontal angle. The most probable exit horizontal angle is $\theta_{I_{max}} = 31°$.

zone of maximum density seems to be between 20° and 25 which is expected form theory and in agreement with the amgle distribution in the simulation.

4.5 Simulation Analysis

In this section, we analyze the data simulated using the Geant4 software, as mentioned before. The simulation consist of 50 fibers at 24 different excitation points each. The results are stored in various text files with ascending job numbers. The excitation points range from $2400mm$ to $100mm$ from the fiber end, spaced $100mm$ apart.

Every entry of the dataset is a single photon travelling through the fiber. The features for each event are:

1. y_{exit}, z_{exit}: Coordinates where the photon exits the fiber (in millimeters).
2. x_{start}, y_{start}, z_{start}: Coordinates where the photon is created (in millimeters).
3. px_{start}, py_{start}, pz_{start}: Momentum components along the axes at the photon's creation. The momentum is normalized meaning $p_x^2 + p_y^2 + p_z^2 = 1$.
4. $refl_{CoCl}$, $refl_{ClCl}$: Number of reflections on the core-cladding and cladding-cladding interfaces.
5. wl: Wavelength of the photon (in nanometers).
6. $gpsPosX$: x-coordinate of the primary particle that excites the fiber (in millimeters).
7. $length_{core}$, $length_{clad}$: Distance traveled in the core or cladding (in millimeters).
8. $rayleighScatterings$: Number of Rayleigh scatterings the photon experienced.

Every entry of the dataset has been categorized into core photon or cladding photon using the feature $refl_{CoCl}$:

- **Core photons**: $refl_{CoCl} > 0$ and $refl_{ClCl} = 0$.
- **Cladding photons**: $refl_{ClCl} > 0$ and $refl_{CoCl} = 0$.

Photons with non-zero values for both $refl_{CoCl}$ and $refl_{ClCl}$ are excluded, enhancing the precision of the categorization. Since these photon consist in 1% of the dataset the data lost is not significant.

To ensure the physical validity of the simulation data, we first corrected any errors by calculating the distance between the fiber's center and the photon's exit point, ensuring it stays within the fiber's geometric bounds ($r_{bound} = 0.125mm$). As illustrated in the histogram in Figure 10, at the distance from the center $0.125mm$ there is a drop in photon counts as we would expect. However there are some photons with exit points outside this bound and, since they are non physical, they were removed.

Next, photons that underwent Rayleigh scattering were also removed from the dataset.

Figure 10: Histogram of reconstructed distances of the photons from the center of the fiber at the exit point.

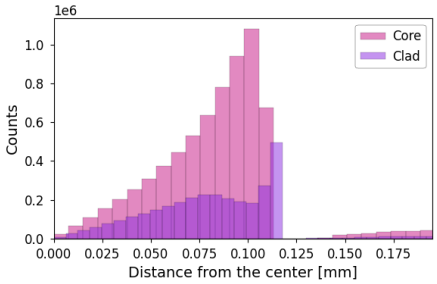

We then investigated the emission angle θ of photons relative to the x-axis of the fiber. The angle θ, since the momentum is normalized, is simply determined from the momentum direction using the equation:

$$\theta = \arcsin(p_x) \tag{9}$$

The distribution of angles for core and cladding photons is shown in Figure 11.

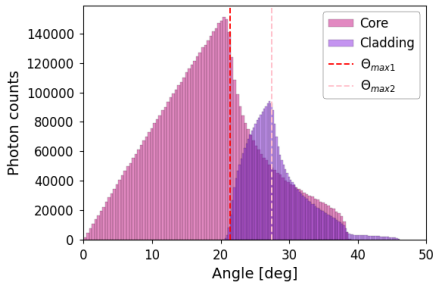

Figure 11: Distribution of emission angles for core and cladding photons. The two theoretical maximum angles of total reflection for core-cladding and cladding-cladding interfaces are shown

In the histogram are also shown the theoretical maximum angle at which total reflection happens for the core-cladding and cladding-cladding interfaces. Applying the Snell law they are simply given by:

$$\theta_{max1} = \arccos(\frac{n_{cl1}}{nco}) \qquad and \qquad \theta_{max2} = arccos(\frac{n_{cl2}}{nco}) \tag{10}$$

Using $n_{co} = 1.60$, $n_{cl1} = 1.49$ and $n_{cl2} = 1.42$ we obtain $\theta_{max1} = 21.4°$ for the core-cladding interface and $\theta_{max2} = 27.4°$ for the cladding-cladding interface.

In the histogram we can clearly see two different behaviour for the distribution:

1. **Linear Rise of Photon Counts:** The linear increase in photon counts from 0° to approximately 20° for the core photons and approximately 27° for the cladding photons can be explained by the optical characteristics of the scintillating fibers. As the angle of incidence increases, the effective surface area of the fiber exposed to incoming photons grows. This geometrical exposure allows a broader range of light angles to enter the fiber, enhancing the initial capture of photons.
2. **Exponential Decrease:** Beyond that threshold value, the graph shows a pronounced exponential decrease in photon counts extending to 50°. This decline is attributed to the inherent limitations of total internal reflection within the fiber. As the angle of incidence exceeds the critical angle, photons no longer undergo total internal reflection efficiently. Instead, they escape the fiber boundary, leading to significant losses in photon counts.

The angle distribution of the simulation is then very convincing since the threshold that separates the linear increase from the exponential decrease seem to correspond precisely to the theoretical maximum angles of total reflection calculated for the two interfaces.

Another important feature to analyze is the minimum distance r_{min} between the fiber's center and the photon's path introduced in Section 3. We stated that considering initial position and the normalized initial momentums we have the equation of the line that describes the initial trajectory of the photon. r_{min} is then the closest distance between this line and the center of the fiber which can be easily shown to be:

$$r_{min} = \frac{|pz_{start}y_{start} - py_{start}z_{start}|}{\sqrt{pz_{start}^2 + py_{start}^2}} \tag{11}$$

Photons with $r_{min} > r_{fiber} = 0.11mm$ were excluded since not physical.

The histogram of the distribution of r_{min} after the cut is shown in Figure 12.

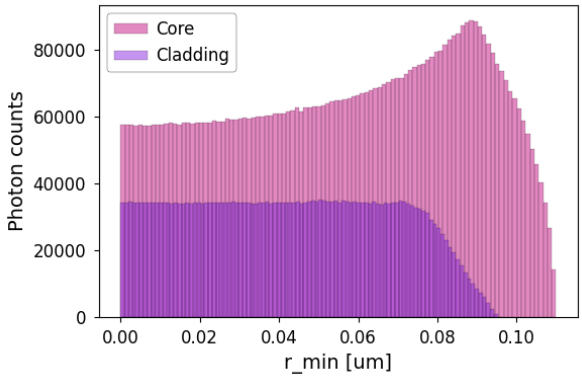

Figure 12: Histogram of r_{min} after excluding external photons.

The distribution of photon counts as a function of the minimum radial distance from the center has a different behaviour for core and cladding photons as expected.

- **Cladding Counts**: The photons count in the cladding are obviously lower than the core counts at every r_{min} since they consider only the photon which were produced with a $\theta > \theta_{max1}$ that makes them go in the cladding without any reflection in the core. They are almost constant until an r_min of $0.08mm$ after which the counts drop. This is because for higher r_{min} the photons move helix like through the fiber and the angle with which they arrive at the interface goes to 0 even for higher θ.
- **Core Counts**: For the same optical reason the core photon counts increases with, since the angle range at which the photon stays in the core is is higher for higher r_{min}. In fact, right when the cladding photon counts drop at $0.8mm$ the core photons encounter a sharp peak. Finally going at r_{min} very close to the core radius the count drops for statistical reason, since they have to be produced very close to the core border.

Finally, the distributions of θ and r_{min} were combined into a 2D heatmap, shown in Figure 13.

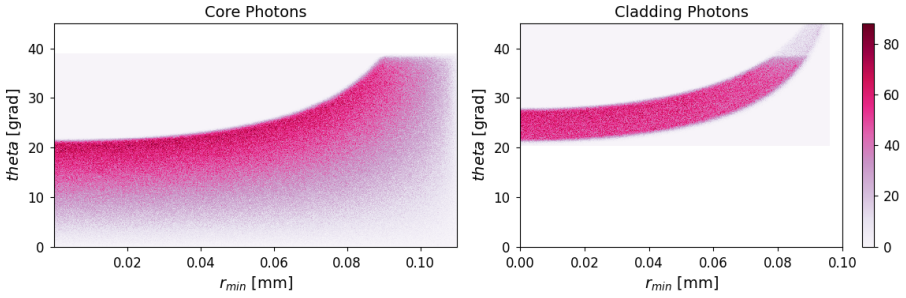

Figure 13: 2D histogram of the photon counts in terms of r_{min} and θ for both core (left) and cladding (right) photons.

The heatmap of the core photons shows a wide range of angles from approximately 0 to 40

degrees. We notice that for low r_{min} the intensity increases until the maximum angle for total reflection (θ_{max1}) then instantly drops as we would expect. While for r_{min} towards $0.10mm$ the intensity increases until higher angles since, as we described in Section 3, for r_{min} close to r_{core} the photons move helix like through the fiber and are reflected even for high θ. The pattern of increasing photon counts near the boundary of the core and cladding highlights the optimal use of the core's refractive properties to maximize light confinement.

For cladding photons instead, as we would expect, we can see a narrower band of angles primarily between θ_{max1} ad θ_{max2}. Angles at which photons arrive in the cladding and are kept in the cladding. The same consideration we made for core photons is then valid, with intensity peaking at higher θ for r_{min} that reaches the fiber's radius. The plots show really well how the cladding function is mainly to minimize photon loss from the core, supporting only specific conditions for photon guidance.

As last step for the simulation analysis the intensity has been valuated for different angles as a function of the excitation location. This has been done using a two-dimensional histogram presented in Figure 14.

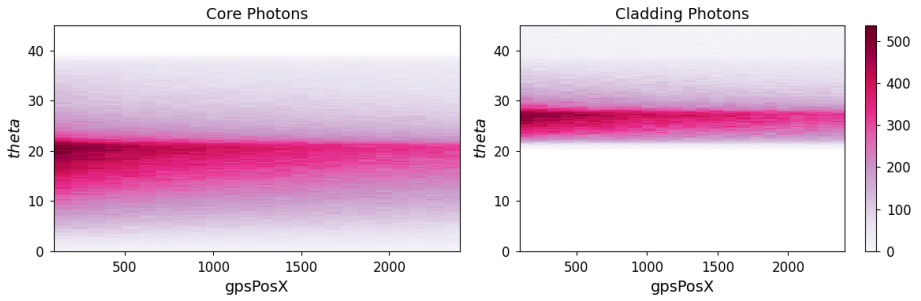

Figure 14: Distribution of the intensity in terms of θ and their excitation position gpsPosX for both the core and cladding photons.

We can see that the heatmap for core photons displays a consistent band of angles, predominantly between 10° and 25° degrees, peaking, as we expect, around 20°. The intensity also slightly decreases as we move at higher gpsPosX since the farther the photon is produced the less probability it has to reach the end of the fiber because of attenuation.

For cladding photons we also have a band of angles, but it is slightly narrower, ranging mainly between 20° and 30°, and peaking around 27°. Like the core distribution, the cladding maintains this range of angles across various positions along the fiber only slightly decreasing with distance. The uniformity in the cladding suggests that, while it handles a narrower range of angles than the core, it still efficiently guides the photons that fall within this range.

As we discussed before the decrease in photon counts with increasing gpsPosX is indicative of attenuation which is due to different mechanisms:

- Absorption by the fiber material itself, which converts the photon energy into non-light energy forms.

- Rayleigh scattering, where photons are scattered by the small imperfections within the fiber material, eventually leading photons to exit the fiber path or lose energy.
- Imperfections or inconsistencies in the fiber, which may become more impactful over distance.

The intensity, as we stated in Section 3, for a fixed θ follows negative exponential function with the distance:

$$I(x) = e^{-ax} \tag{12}$$

where a is the attenuation coefficient.
By fixing a range of angles, we can represent the intensity in terms of the excitation position for that range of angles and perform an exponential fit to obtain a for the specific angle region. A few example of choice of angle ranges are presented in Figure 15.

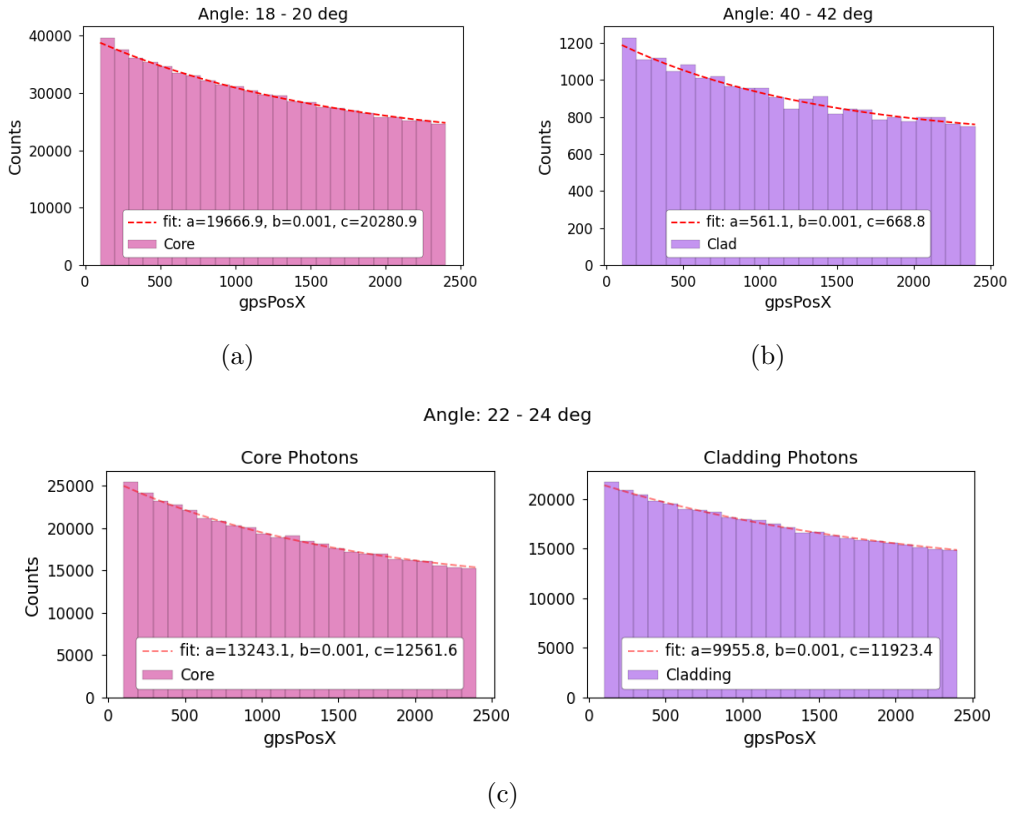

(a) (b)

(c)

Figure 15: Attenuation coefficient as a function of angle. (a) Core photons for $22° < \theta < 24°$, (b) Core and cladding photons for $44° < \theta < 46°$, (c) Cladding photons for $22° < \theta < 24°$.

Specifically, we chose $18° < \theta < 20°$ in which only core photons appear (see Figure 15, panel (a)). Then the range $40° < \theta < 42°$ in which only cladding photons appear (see Figure 15, panel (b)). Then, we performed a double fit for core and cladding photons in an angular region where we have counts for both cladding and core photons: $22° < \theta < 24°$ (see Figure 15, panel (c)).
Since the fits have been performed using the following exponential function:

$$p1 \cdot e^{-p2 \cdot x} + p3 \tag{13}$$

in order to get the attenuation coefficient we used the following $a = p2$.

The plot of a with respect to the angles is finally shown in the Figure 16. For this plot we choose to

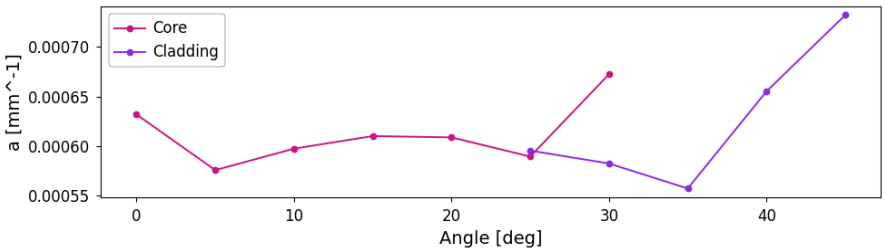

Figure 16: Plot of the attenuation coefficient in terms of the angle.

Theoretically, we expect that photons with higher angles, having traveled a longer path, have more probability of scattering and absorption leading to an higher attenuation of the intensity. The plot, however, does not show a constant increase with the angle, specifically for low angles. This could be due to some inaccuracies in the simulation. Nevertheless we notice an increasing tendencies of a towards higher angles, especially for cladding photons.

5 Conclusion

This study provides a comprehensive analysis of scintillating fibers, focusing on their application within the LHCb experiment. The dual approach of experimental measurements and Monte Carlo simulations has yielded several critical insights into the behavior of photons within these fibers. This analysis ensures that the simulation data aligns with the expected physical properties of the scintillating fibers, providing a reliable basis for further studies and optimizations in fiber design and particle tracking applications.

The experimental results validate the fundamental characteristics of scintillating fibers. The radial symmetry of the fiber's response and the intensity measurements across various angles confirm the expected photon distribution patterns. This consistency underscores the reliability of scintillating fibers in tracking charged particles with high precision.

The Monte Carlo simulations conducted using Geant4 provide a deeper understanding of the photon transport mechanisms within the fibers. The angle distributions of core and cladding photons closely match the theoretical maximum angles for total reflection, confirming the accuracy of the simulation model. The analysis of the minimum distance r_{min} between the fiber's center and the photon paths further supports the validity of the simulation, as the distributions align with expected physical behaviors.

The simulation also reveals the complex interplay between various factors affecting photon transport, including reflections at core-cladding interfaces and attenuation due to absorption and scattering. The attenuation coefficient, determined through both experimental and simulation data, remains relatively consistent, although some discrepancies suggest areas for further refinement in the simulation model.

Overall, this study provides a comprehensive analysis of scintillating fibers, focusing on their application within the LHCb experiment.

References

[1] LHCb Collaboration. Lhcb scintillating fibre tracker engineering design review report: Fibres, mats and modules, 2015. LHCb-PUB-2015-008.

[2] A. A. Alves Jr. et al. (LHCb Collaboration). The lhcb detector at the lhc. *Journal of Instrumentation*, 3(S08005), 2008.

[3] R. Aaij et al. (LHCb Collaboration). The lhcb detector at the lhc. *Journal of Instrumentation*, 9(08):P08005, 2014.